Highly Silicic Compositions on the Moon

Timothy D. Glotch,[1]* Paul G. Lucey,[2] Joshua L. Bandfield,[3] Benjamin T. Greenhagen,[4]
Ian R. Thomas,[5] Richard C. Elphic,[6] Neil Bowles,[5] Michael B. Wyatt,[7] Carlton C. Allen,[8]
Kerri Donaldson Hanna,[6] David A. Paige[9]

Using data from the Diviner Lunar Radiometer Experiment, we show that four regions of the Moon previously described as "red spots" exhibit mid-infrared spectra best explained by quartz, silica-rich glass, or alkali feldspar. These lithologies are consistent with evolved rocks similar to lunar granites in the Apollo samples. The spectral character of these spots is distinct from surrounding mare and highlands material and from regions composed of pure plagioclase feldspar. The variety of landforms associated with the silicic spectral character suggests that both extrusive and intrusive silicic magmatism occurred on the Moon. Basaltic underplating is the preferred mechanism for silicic magma generation, leading to the formation of extrusive landforms. This mechanism or silicate liquid immiscibility could lead to the formation of intrusive bodies.

Spectroscopically unique features that occur on the nearside of the Moon within the Procellarum KREEP Terrane (PKT) (Fig. 1) have been investigated for more than three decades (1–4). Remote sensing data from these localities, known as red spots, are generally characterized by deep ultraviolet (UV) absorptions with respect to the near-infrared (NIR) as well as low FeO and TiO₂ concentrations. The unusual spectral characteristics of the Gruithuisen Dome red spots, which also have steep slopes (15° to 30°) and rough surface textures suggest that they formed from feldspathic magmas with high silica contents, similar to terrestrial rhyolite domes (3, 5, 6). Recent analyses suggest that four red spots—Hansteen Alpha, the Gruithuisen Domes, the Lassell Massif, and Aristarchus Crater—have elevated Th and low FeO abundances, suggesting derivation from evolved magmas (7, 8). None of the previously applied techniques, including UV/visible/NIR (UV/VIS/NIR) spectroscopy and gamma-ray spectroscopy (GRS), are directly sensitive to the key indicators of silicic volcanism (quartz, silica-rich glass, and alkali and ternary feldspars). Therefore, unambiguous identification of the composition of these features has not previously been possible.

The Diviner Lunar Radiometer Experiment on the Lunar Reconnaissance Orbiter is a multispectral radiometer that is well suited to detecting the mineral indicators of silicic volcanism. Diviner has three narrow spectral bandpass filters centered at 7.8, 8.25, and 8.55 μm (channels 3 to 5). These three "8-μm" channels were specifically designed to characterize the position of the Christiansen Feature (CF) (9, 10), which is directly sensitive to silicate mineralogy and the bulk SiO₂ content of a material (11–15).

We have compared the mid-IR spectral shapes of lunar red spots to those of the surrounding mare and highlands, which are regions suggested to be pure plagioclase feldspar, based on SELENE Multiband Imager data (16); and the laboratory emissivity spectra of minerals and rocks acquired in a simulated lunar environment (15). The available data cover portions of Hansteen Alpha, the Lassell Massif region, the Gruithuisen Gamma and Northwest Domes, Aristarchus Crater, Southern Montes Riphaeus, and Helmet red spots.

Silicic minerals and lithologies exhibit short-wavelength position CFs. The response of the Diviner 8-μm channels to this characteristic is to show a strong positive slope in three-point spectra toward short wavelengths with a weak curvature. Convolved to the Diviner bandpasses, quartz and silica-rich materials such as obsidian glass and alkali feldspar have three-point spectra that are strongly concave upward. Moderate-composition feldspars such as labradorite are weakly concave upward, whereas anorthite and more typical lunar materials that are mafic to ultramafic (anorthite, pyroxene, olivine, and mixtures thereof) show strongly concave-downward spectra (Fig. 2). The combination of spectral slope and concavity in the Diviner 8-μm channels are strongly tied to the silica content of a material and can be used to identify Si-rich compositions.

To map variations in silicate mineralogy, we defined two spectral parameters to describe the Diviner three-point spectra. The first spectral index, I, measures the slope between channels 3 and 4 in the form $I = \varepsilon 3 - \varepsilon 4$, where $\varepsilon 3$ and $\varepsilon 4$ are the emissivities in channels 3 and 4, respectively. A second spectral index, c, determines the direction of concavity between channels 3 and 5 (17). A positive value of this index is indicative of a concave-up shape, whereas a negative index value is indicative of a concave-down shape.

Hansteen Alpha, the Lassell Massif region, the Gruithuisen Domes, and the southern rim and ejecta blanket of Aristarchus each have I parameter values that are substantially higher than those of the surrounding highlands material in each region. Portions of each of these features also display positive c (concave-up) index values (Fig. 3 and Table 1).

Comparison to laboratory spectra acquired under simulated lunar conditions and convolved with the Diviner bandpasses indicates that anorthite and all minerals more silicic than it have positive I parameter values. Only the most-silicic materials, containing substantial amounts of Si-rich glass, quartz, and/or alkali feldspars, display strongly concave-up spectral character, although labradorite is also weakly concave-up (Fig. 2). The CF positions of these materials occur at wavelengths well short of the Diviner 8-μm channels. Other regions in each of these red spots have negative concavity index values but positive I parameter values. The average calculated CF position for these concave-down spectral shapes, modeled in the manner of (10), is 7.87 μm (1271 cm⁻¹), which is consistent with a mixture of the silicic composition with more mafic components.
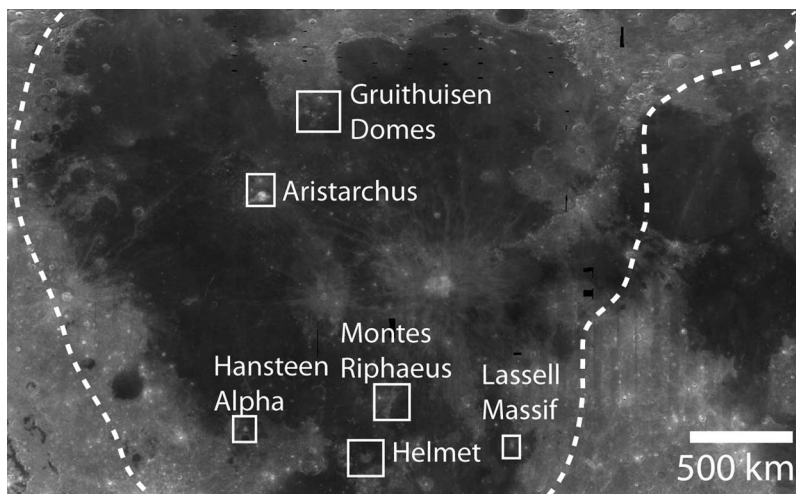
[1]Department of Geosciences, Stony Brook University, Stony Brook, NY, USA. [2]Hawaii Institute of Geophysics and Planetology, University of Hawaii, Hawaii, HI, USA. [3]Department of Earth and Space Sciences, University of Washington, Seattle, WA, USA. [4]Jet Propulsion Laboratory, California Institute of Technology, 4800 Oak Grove Drive, Pasadena, CA 91109–8099, USA. [5]Department of Physics, University of Oxford, Oxford, UK. [6]NASA Ames Research Center, Moffett Field, CA 94035–1000, USA. [7]Department of Geological Sciences, Brown University, Providence, RI, USA. [8]NASA Johnson Space Center, Houston, TX 77058, USA. [9]Department of Earth and Space Sciences, University of California, Los Angeles, Los Angeles, CA, USA.

*To whom correspondence should be addressed. E-mail: tglotch@notes.cc.sunysb.edu

Fig. 1. Clementine 750-nm mosaic showing the locations of the features discussed in the text. The outline marks the boundary of the PKT as defined by (32).

Three-point spectra of each of the red spots are distinct from those of the surrounding terrain. Both mare and highlands materials in each region have spectral shapes with negative concavity and slope index values. The average CF positions of local mare and highlands material in each region are 8.33 and 8.19 μm, respectively, which compare well with those derived from the global data set (10).

The regions previously interpreted to be the most silicic on the Moon have been classified as nearly pure anorthite, based on VIS/NIR spectral observations (16, 18). The spectral properties of these areas are key to our interpretation of the presence of even more-silicic minerals, indicating evolved lithologies. Diviner spectra of pure plagioclase from the inner ring of the Orientale multi-ring impact basin are concave-down with a positive slope index (Fig. 4), and the modeled CF position is 7.89 μm, which is similar to that derived for the red-spot mixed lithologies. Of all the feldspars, anorthite has the longest-wavelength CF position, and this comparison indicates that red spots with CF positions shorter than those of areas interpreted to be pure anorthite, along with positive I parameter and c index values, are largely composed of quartz, Si-rich glass, and alkali feldspars, or mixtures thereof.

The concave-upward shapes and positive slope indices in the spectra of Hansteen Alpha, Lassell Massif, the Gruithuisen Domes, and the southern rim and ejecta of Aristarchus Crater indicate the presence of highly silicic evolved lithologies. Evolved compositions are also consistent with strong positive anomalies of Th, an incompatible large-ion lithophile element (7, 8). Red spots that lack high Th anomalies also lack the concave-up spectral character in Diviner data, confirming a lack of silicic indicator minerals. These include the Helmet Feature, Darney Chi, Darney Tau, Montes Riphaeus, and Mons La Hire. Spectra of the Helmet Feature and Montes Riphaeus display concave-down shapes and have negative slope parameters (Fig. 4) and are generally indistinguishable from the surrounding highlands in the Diviner data (Fig. 3) (19). The distribution of high-Si compositions is spatially correlated with the Th anomalies in Lunar Prospector Gamma-Ray Spectrometer (GRS) data (8, 9) and low FeO abundance derived from Clementine UV/VIS/NIR imagery (20, 21). Red spots lacking a silicic composition have typical Th and FeO abundances.

The four silicic features described here have variable geologic settings that probably represent both extrusive and intrusive igneous processes. The Gruithuisen Domes and Hansteen Alpha have previously been proposed to be silicic volcanic constructs (3, 5, 6, 22). The compositions as determined by Diviner are consistent with previous interpretations of these features resulting from silicic extrusive volcanic processes. The Aristarchus and Lassell regions appear to be sampling silicic lithologies emplaced at depth. The Si-rich materials at Aristarchus are confined to the southern rim and ejecta of Aristarchus Crater, whereas the thick blanket of TiO_2-poor pyroclastic materials that covers much of the Aristarchus Plateau (23, 24) does not have a silicic spectral signature in Diviner data. This suggests that Aristarchus Crater exposed an intrusive silicic lithology. Alternatively, the Aristarchus cratering event could have exposed an extrusive lithology that was subsequently buried by mare lavas and the pyroclastic deposits of the Aristarchus Plateau. The silicic materials in the Lassell region (Fig. 3e) are associated with an ~50 × 20–km patch of highlands material (the

Fig. 2. Full-resolution (2 cm⁻¹ spectral sampling) laboratory spectra of major rock-forming minerals and those spectra convolved to the Diviner channel-3 to -5 bandpasses. Arrows mark the position of the silicate CF. Microcline does not display a strong CF.
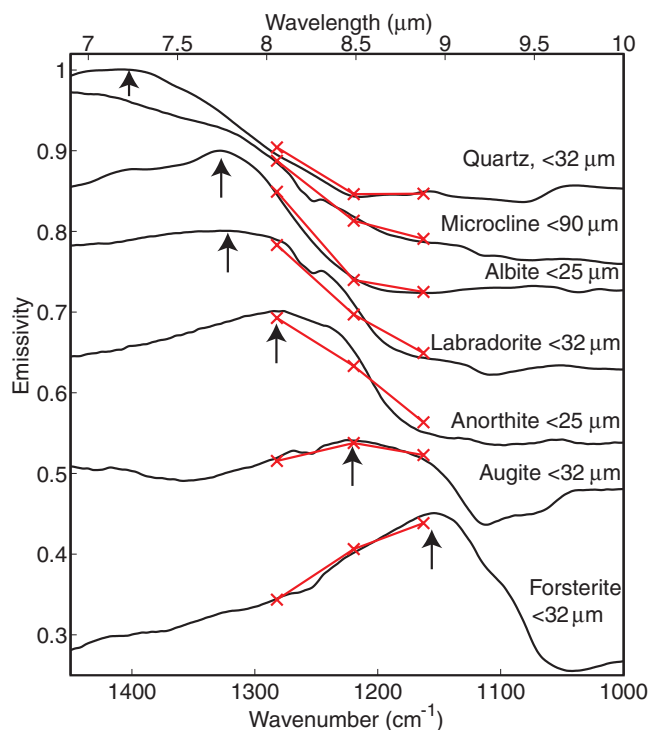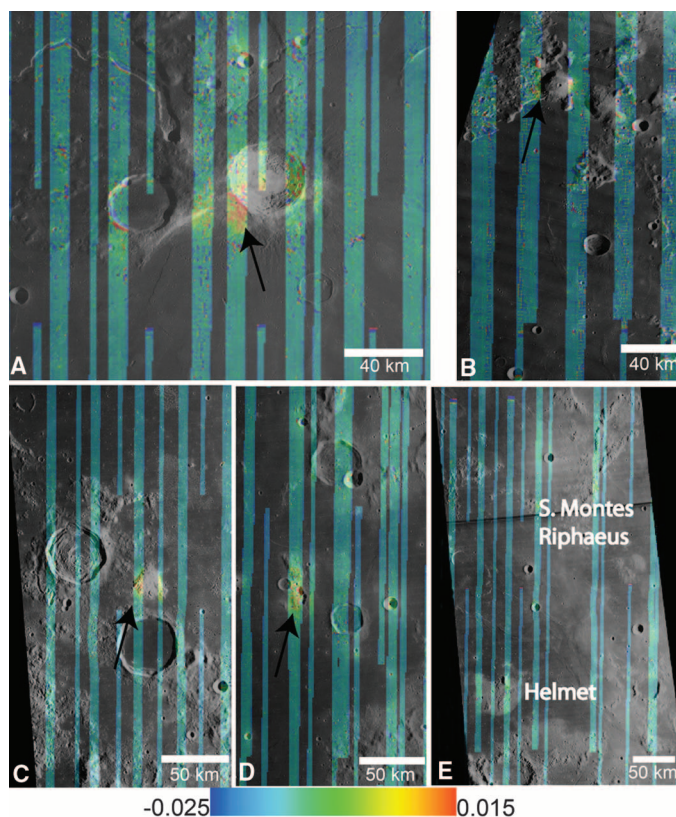

Fig. 3. Concavity index maps overlaid on digitized Lunar Orbiter IV images. High values of the index (red) indicate increasingly silicic compositions. (**A**) Aristarchus Crater. (**B**) Gruithuisen Domes. (**C**) Hansteen Alpha. (**D**) Lassell. (**E**) Helmet and Southern Montes Ripheus.

Lassell Massif) and the small impact craters Lassell K, G, and C (*25*). The direct association of the silicic signature with the impact craters at the Lassell site suggests that it is due to the exposure of plutonic material or a thick sequence of buried extrusive lavas sampled at depth.

Silicic lithologies on the Moon probably occur as both intrusive plutons and extrusive lavas. Extrusive silicic volcanism, which is likely to have formed Hansteen Alpha and the Gruithuisen Domes, occurred in the Late Imbrian epoch be-

fore most mare volcanism occurred (*22*, *25*, *26*). Mare lavas embay these likely volcanic edifices, indicating that they were once more extensive. The mechanisms for forming highly evolved lithologies are a subject for debate. Small fragments of lunar granite/felsite are present in Apollo soil samples, and age dating gives crystallization ages that span a range of 500 million years (*27*), indicating that magmatic processes capable of producing highly evolved compositions occurred over an extended period of time. Two basic mod-

els have been proposed to account for the presence of highly evolved compositions on the Moon. Silicate liquid immiscibility is a mechanism that has been proposed to be responsible for the origin of the Apollo granite/felsite grains (*28*). It requires that a basaltic magma undergo nearly complete fractional crystallization before the single residual melt separates into two immiscible melts: one that is SiO_2-poor and FeO rich, and one that is rich in SiO_2 and alkalis. It is unlikely that the silicic lavas produced from the small amount of residual melt produced by this process could form large volcanic structures such as the Gruithuisen Domes or Hansteen Alpha (*7*). It is possible, however, that large granitic plutons could have been produced within the lunar crust as a result of the slow crystallization of late-stage magma ocean residual melt (*29*, *30*). This slow cooling method would preclude the formation of large volumes of extrusive lavas (*7*), but it is a reasonable scenario for the formation of large granitic bodies that could be exposed by impact craters.

A second mechanism that could produce large volumes of silicic melt is basaltic underplating, in which a hot basaltic magma intrudes into the lunar crust, causing melting of the anorthositic crust and the generation of silicic magmas (*7*). This process can produce large volumes of buoyant silicic magmas that rise to the surface as rhyolite plumes (*31*). As previously suggested, the thin crust, high abundance of heat-producing elements, and large-scale basaltic magmatism in the PKT all favor the basaltic underplating hypothesis (*7*). Because all four silicic regions discussed in this work occur within the PKT, this mechanism for silicic melt production should be strongly considered.

These four silicic regions have distinctly different geologic settings. The Gruithuisen Domes and Hansteen Alpha are probably the result of extrusive silicic volcanism (*5*, *6*, *22*). Silicic materials have also been exposed by impact craters in the Aristarchus and Lassell regions, perhaps indicating the formation of silicic plutons at depth. Taken together with the proposed magmatic processes, Diviner data point to multiple igneous processes occurring over a sustained period of time, resulting in the formation of silica and rare earth element–enriched compositions on the Moon.

Table 1. Characteristics of features discussed in the text. Dashes indicate that no CF position was calculated.

Feature	Modeled CF*	c	l	Surface temperature	Th (ppm)†
Hansteen Alpha (c > 0)	—	0.00514	0.0217	381.4	6
Hansteen Alpha (c < 0)	7.98	−0.00535	0.0041	381.9	6
Hansteen Mare	8.36	−0.01471	−0.0275	386.4	5
Hansteen Highlands	8.29	−0.01300	−0.0202	379.2	3
Lassell (c > 0)	—	0.00651	0.0256	375.3	11
Lassell (c < 0)	7.69	−0.00564	0.0076	372.9	11
Lassell Highlands	8.12	−0.01184	−0.0124	374.0	4
Lassell Mare	8.31	−0.01324	−0.0225	379.9	7
Gruithuisen Gamma (c > 0)	—	0.00448	0.0139	356.0	10
Gruithuisen Gamma (c < 0)	7.93	−0.01048	0.0019	358.5	10
Gruithuisen NW (c > 0)	—	0.02935	0.0462	360.4	10
Gruithuisen Mare	8.29	−0.01462	−0.0224	345.3	7
Gruithuisen Highlands	8.15	−0.01111	−0.0091	330.7	13
Aristarchus Crater (c > 0)	—	0.00797	0.0339	371.8	14
Aristarchus Crater (c < 0)	7.72	−0.00459	0.0112	377.4	14
Aristarchus Plateau	8.25	−0.01344	−0.0208	375.5	11
Helmet	8.20	−0.01010	−0.0113	379.1	4
Helmet Mare	8.36	−0.01443	−0.0286	382.0	4
Southern Montes Riphaeus	8.09	−0.00634	−0.0028	377.2	5

*CF positions for spectra with positive concavity index values cannot be calculated in the manner of (*10*). †Small-region Th values [in parts per million (ppm)] are based on the deconvolved abundances determined by (*33*).
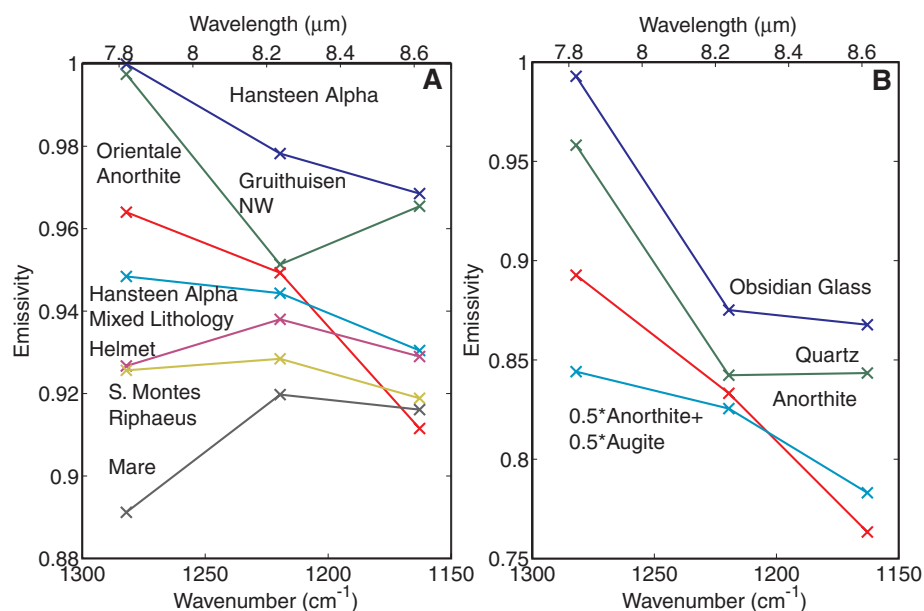

Fig. 4. Diviner and laboratory three-point spectra. (**A**) Spectra from select regions discussed in the text. (**B**) Laboratory spectra convolved to Diviner spectral resolution.

References and Notes
1. E. A. Whitaker, *Moon* **4**, 348 (1972).
2. M. Malin, *Earth Planet. Sci. Lett.* **21**, 331 (1974).
3. J. W. Head 3rd, T. B. McCord, *Science* **199**, 1433 (1978).
4. B. C. Bruno *et al.*, *Proc. Lunar Planet. Sci. Conf.* **21**, 405 (1991).
5. J. W. Head *et al.*, *Lunar Planet. Sci.* **IX**, 488 (abstract) (1978).
6. S. D. Chevrel, P. C. Pinet, J. W. Head, *J. Geophys. Res.* **104**, 16,515 (1999).
7. J. J. Hagerty *et al.*, *J. Geophys. Res.* **111**, E06002 (2006).
8. J. J. Hagerty *et al.*, *J. Geophys. Res.* **114**, (2009).
9. D. A. Paige *et al.*, *Space Sci. Rev.* **150**, 125 (2009).
10. B. T. Greenhagen *et al.*, *Science* **329**, 1507 (2010).
11. J. E. Conel, *J. Geophys. Res.* **74**, 1614 (1969).
12. L. M. Logan, G. R. Hunt, J. W. Salisbury, S. R. Balsamo, *J. Geophys. Res.* **78**, 4983 (1973).
13. J. W. Salisbury, L. S. Walter, *J. Geophys. Res.* **94**, 9192 (1989).

14. The CF occurs in the portion of the mid-IR spectrum where the real part of the complex refractive index is changing rapidly and approaching that of the surrounding medium, resulting in minimal scattering and an emissivity maximum.
15. Materials and methods are available as supporting material on *Science* Online.
16. P. D. Spudis, B. R. Hawke, P. Lucey, *J. Geophys. Res.* **89**, C197 (1984).
17. We defined a line using channels 3 and 5 and interpolated the value of the channel 4 emissivity on this line. We then subtracted the true channel-4 emissivity from this value.
18. M. Ohtake *et al.*, *Nature* **461**, 236 (2009).
19. Diviner data meeting our analysis criteria have not been acquired over Mons La Hire, Darney Chi, or Darney Tau.
20. P. G. Lucey, G. J. Taylor, E. Malaret, *Science* **268**, 1150 (1995).
21. P. G. Lucey, D. T. Blewett, B. R. Hawke, *J. Geophys. Res.* **103**, 3679 (1998).
22. B. R. Hawke *et al.*, *J. Geophys. Res.* **108**, 5069 (2003).
23. P. G. Lucey, B. R. Hawke, C. M. Pieters, J. W. Head, T. B. McCord, *J. Geophys. Res.* **91** (suppl.), D344 (1986).
24. B. B. Wilcox, P. G. Lucey, B. R. Hawke, *J. Geophys. Res.* **111**, E09001 (2006).
25. C. A. Wood, J. W. Head, *Conference on the Origin of Mare Basalts* (Lunar Science Institute, Houston, TX, 1975).
26. R. Wagner *et al.*, *Lunar Planet. Sci.* **XXVII**, 1367 (abstract) (1996).
27. L. E. Nyquist, C. Y. Shih, *Geochim. Cosmochim. Acta* **56**, 2213 (1992).
28. B. L. Jolliff *et al.*, *Am. Mineral.* **84**, 821 (1999).
29. C. R. Neal, L. A. Taylor, *Geochim. Cosmochim. Acta* **53**, 529 (1989).
30. B. L. Jolliff, *Int. Geol. Rev.* **40**, 916 (1998).
31. S. Maaløe, A. R. McBirney, *J. Volcanol. Geotherm. Res.* **76**, 111 (1997).
32. B. L. Jolliff, J. J. Gillis, L. A. Haskin, R. L. Korotev, M. A. Wieczorek, *J. Geophys. Res.* **105**, 4197 (2000).
33. D. J. Lawrence *et al.*, *J. Geophys. Res.* **105**, 20307 (2000).
34. This work was funded in part by the Diviner science budget. T.D.G., J.L.B., M.B.W., and R.C.E. were supported by the NASA Lunar Reconnaissance Orbiter Participating Scientist program.

Rainforest Aerosols as Biogenic Nuclei of Clouds and Precipitation in the Amazon

U. Pöschl,[1]* S. T. Martin,[2]* B. Sinha,[1] Q. Chen,[2] S. S. Gunthe,[1] J. A. Huffman,[1] S. Borrmann,[1] D. K. Farmer,[3] R. M. Garland,[1] G. Helas,[1] J. L. Jimenez,[3] S. M. King,[2] A. Manzi,[4] E. Mikhailov,[1,5] T. Pauliquevis,[6,7] M. D. Petters,[8,9] A. J. Prenni,[8] P. Roldin,[10] D. Rose,[1] J. Schneider,[1] H. Su,[1] S. R. Zorn,[1,2] P. Artaxo,[6] M. O. Andreae[1]

The Amazon is one of the few continental regions where atmospheric aerosol particles and their effects on climate are not dominated by anthropogenic sources. During the wet season, the ambient conditions approach those of the pristine pre-industrial era. We show that the fine submicrometer particles accounting for most cloud condensation nuclei are predominantly composed of secondary organic material formed by oxidation of gaseous biogenic precursors. Supermicrometer particles, which are relevant as ice nuclei, consist mostly of primary biological material directly released from rainforest biota. The Amazon Basin appears to be a biogeochemical reactor, in which the biosphere and atmospheric photochemistry produce nuclei for clouds and precipitation sustaining the hydrological cycle. The prevailing regime of aerosol-cloud interactions in this natural environment is distinctly different from polluted regions.

Atmospheric aerosols are key elements of the climate system. Depending on composition and abundance, aerosols can influence Earth's energy budget by scattering or absorbing radiation and can modify the characteristics of clouds and enhance or suppress precipitation. The direct and indirect aerosol effects on climate are among the largest uncertainties in the current understanding of regional and global environmental change. A crucial challenge is developing a quantitative understanding of the sources and properties of aerosol particles, including primary emission from the Earth's surface, secondary formation in the atmosphere, chemical composition and mixing state, and the ability to nucleate cloud droplets and ice crystals—all as influenced by human activities as compared with natural conditions (1–4).

During the wet season, the Amazon Basin is one of the few continental regions where aerosols can be studied under near-natural conditions (5–7). The Amazonian Aerosol Characterization Experiment 2008 (AMAZE-08) was conducted in the middle of the wet season at a remote site north of Manaus, Brazil (February to March 2008), and the investigated air masses came with the trade wind circulation from the northeast over some 1600 km of pristine tropical rainforest (8). Here, we focus on measurements performed in the period of 3 to 13 March 2008, when the influence of long-range transport from the Atlantic Ocean, Africa, or regional anthropogenic sources of pollution was particularly low and the aerosol properties were dominated by particles emitted or formed within the rainforest ecosystem (6, 7, 9, 10). The measurement techniques applied include scanning electron microscopy (SEM) with energy-dispersive x-ray spectroscopy (EDX), atomic force microscopy (AFM), secondary ion mass spectrometry (NanoSIMS), aerosol mass spectrometry (AMS), differential mobility particle sizing (DMPS), ultra-violet aerodynamic particle sizing (UV-APS), and counting of cloud condensation nuclei (CCN) and ice nuclei (IN) (8). To our knowledge, this study provides the first comprehensive, detailed, and size-resolved account of the chemical composition, mixing state, CCN activity, and IN activity of particles in pristine rainforest air approximating pre-industrial conditions (5–7).

SEM images of characteristic particle types are shown in Fig. 1. Nearly all detected particles could be attributed to one of the following five categories: (i) secondary organic aerosol (SOA) droplets that were formed by atmospheric oxidation and gas-to-particle conversion of biogenic volatile organic compounds (9) and in which no other chemical components were detectable; (ii) SOA-inorganic particles composed of secondary organic material mixed with sulfates and/or chlorides from regional or marine sources (6); (iii) primary biological aerosol (PBA) particles, such as plant fragments or fungal spores (6, 11, 12); (iv) mineral dust particles consisting mostly of clay minerals from the Sahara desert (6, 13); or (v) pyrogenic carbon particles that exhibited characteristic agglomerate structures and originated from regional or African sources of biomass burning or fossil fuel combustion (6). In mixed SOA-inorganic particles, the organic fraction was typically larger than the inorganic fraction. The primary biological, mineral dust, and pyrogenic carbon particles were also partially coated with organic material [supporting online material (SOM) text].

The average number and mass size distribution, composition, and mixing state of particles as detected with microscopy and complementary online measurements are shown in Fig. 2. The online instruments measure different types of equivalent diameters, which can vary depending on the shape and the density of the particles. Nevertheless, the size distribution patterns obtained with the different techniques are in overall agreement with each other. SEM is the one method that cov-

[1]Max Planck Institute for Chemistry, 55128 Mainz, Germany. [2]School of Engineering and Applied Sciences and Department of Earth and Planetary Sciences, Harvard University, Cambridge, MA 02138, USA. [3]Department of Chemistry and Biochemistry and Cooperative Institute for Research in Environmental Science, University of Colorado, Boulder, CO 80309, USA. [4]National Institute of Amazonian Research, 69060 Manaus, Brazil. [5]Atmospheric Physics Department, Institute of Physics, St. Petersburg State University, 198904 St. Petersburg, Russia. [6]Institute of Physics, University of São Paulo, 05508 São Paulo, Brazil. [7]Federal University of São Paulo, 04023 Diadema, Brazil. [8]Department of Atmospheric Science, Colorado State University, Fort Collins, CO 80523, USA. [9]Marine Earth and Atmospheric Science, North Carolina State University, Raleigh, NC 27695, USA. [10]Department of Physics, Lund University, 22100 Lund, Sweden.

*To whom correspondence should be addressed. E-mail: u.poschl@mpic.de (U.P.); scot_martin@harvard.edu (S.T.M.)